Optical Engineering

SPIEDigitalLibrary.org/oe

Ultrafast reflection and secondary ablation in laser processing of transparent dielectrics with ultrashort pulses

Mingying Sun
Urs Eppelt
Wolfgang Schulz
Jianqiang Zhu

Ultrafast reflection and secondary ablation in laser processing of transparent dielectrics with ultrashort pulses

Mingying Sun,[a,b,c] Urs Eppelt,[b,c] Wolfgang Schulz,[b,c] and Jianqiang Zhu[a,*]
[a]Shanghai Institute of Optics and Fine Mechanics, Chinese Academy of Sciences, No. 390, Qinghe Road, Jiading District, Shanghai 201800, China
[b]Fraunhofer Institute for Laser Technology, Steinbachstraße 15, 52074 Aachen, Germany
[c]RWTH Aachen University, Nonlinear Dynamics of Laser Processing, Steinbachstraße 15, 52074 Aachen, Germany

Abstract. Ultrafast reflection and secondary ablation have been theoretically investigated with a Fresnel-Drude model in laser processing of transparent dielectrics with picosecond pulsed laser. The time-dependent refractive index has a crucial effect on the cascade ionization rate and, thereby, on the plasma generation. The relative roles of the plasma gas and the incident angle in the reflection are discussed in the case of the oblique incidence. The angular dependence of the reflectivity on the laser-excited surface for s- and p-polarization is significantly different from the usual Fresnel reflectivity curve in the low-fluence limit. A road map to the secondary ablation induced by the reflected pulse is obtained on the angles of the first and second incidence. It indicates that the laser-induced plasma plays a major role in the secondary ablation, which could overcome the saturation of the ablation crater depth or generate microcracks underneath the crater wall. [DOI: 10.1117/1.OE.53.5.051512]

Keywords: laser-induced breakdown; laser ablation; ultrafast lasers; nonlinear reflectivity.

Paper 131178SS received Aug. 1, 2013; revised manuscript received Dec. 19, 2013; accepted for publication Dec. 24, 2013; published online Jan. 27, 2014.

1 Introduction

Ultrashort pulsed laser ablation has been used in micromachining of transparent dielectrics,[1,2] such as laser cutting[3,4] and channeling[5–8] for many years. One of the issues that has significant influence on the processing quality is the secondary ablation (SDA) induced by the reflected laser pulse. When an ultrashort laser pulse interacts with the dielectric material, free electrons are generated via multiphoton ionization (MPI) and cascade ionization (CI).[9] The dense plasma results in great changes of the refractive index and the surface reflectivity. When laser-induced plasma density reaches the critical value $\rho_{\mathrm{crit}} = (\omega^2 m_e \varepsilon_0)/e$ dependent on the laser frequency, it gets highly absorbing and reflective[10–14] and a large portion of the laser pulse energy is deposited on the dielectrics surface. Energy transfer from the free electrons to the atomic subsystem (lattice) will cause bond breaking and material expansion.[3] Due to these ablation behaviors, an ablated crater is generated. As the crater depth increases, the sidewall becomes steeper[6–8] and the angle of incidence on the sloped wall for subsequent pulses increases from 0 deg until the projection of the incident intensity on the wall drops below the ablation threshold (ablation stop). This temporary stop of ablation might then be overcome due to the reflection of the incoming pulse and reabsorption at an incident angle smaller than the critical angle corresponding to the ablation threshold. This leads to an ablation beyond the usual ablation stop. On the other hand, it could also lead to an additional damage of the dielectric substrate.

Dense plasma[10–14] and large angles of incidence[15] both affect the reflection of the laser pulse on the crater sidewall. The schematic diagram of SDA is shown in Fig. 1. The laser pulse reflected by the laser-induced plasma in the primary ablation on the dielectric surface S2 will irradiate the opposite crater wall (surface S4) and could induce SDA and generate some damage, such as microcracks[5] and ablation craters.[7] SDA induced by the primary ablated particles[16] has been studied by molecular dynamics simulations. The SDA induced by the reflected pulse, however, requires a deep understanding of the nonlinear absorption mechanism.

In this paper, we study the transient behaviors of nonlinear reflectivity and SDA in ultrafast laser ablation with a Fresnel-Drude model. First, the reflection behaviors at different fluences and different incident angles are numerically investigated, respectively. Second, the angular dependences of reflectivity for laser pulses are calculated and compared to the Fresnel reflectivity curves. At the same time, SDA induced by the reflected and shaped pulse on the sample is analyzed. At last, a road map to SDA is shown on the angles of the first and second incidence for different laser fluences.

2 Physical Process and Definition

As shown in Fig. 1, a laser pulse with a fluence of F is incident on the sloped surface S2 of the ablated crater with an incident angle of θ_i; thus the effective fluence on the surface S2 is $F \cos \theta_i$ because of the projection effect. In this work, for simplicity, we only consider the reflection at the spot center of the laser beam, where the maximum intensity is located and laser ablation happens first. If one wants to get the reflectivity of the laser beam measured in the experiment, the distribution of laser beam on the transverse plane

*Address all correspondence to: Jianqiang Zhu, E-mail: jqzhu@mail.shcnc.ac.cn

0091-3286/2014/$25.00 © 2014 SPIE

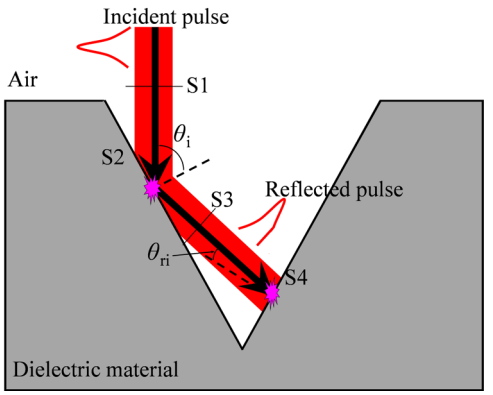

Fig. 1 Schematic diagram of the secondary ablation. θ_i is the angle of incidence of the incoming pulse and θ_{ri} is the angle of incidence of the reflected pulse on the opposite wall. S1, S2, S3, and S4 are four planes where the laser intensity is measured. When the laser fluence is larger than the ablation threshold, because of the absorption on the surface S2, the reflected pulse is modified to be in a Gaussian-like shape with a cut-off front ramp and irradiates on the surface S4.

has to be taken into account in the calculation of the reflectivity. The intensity distribution of the initial laser pulse on the surface S1, which is perpendicular to the axis of the incident beam, is a Gaussian profile $I(t) = I_0 \exp[-4 \ln 2(t/t_p)^2]$, where t_p is the pulse duration and I_0 is the peak intensity on the surface S1 given by

$$I_0 = \frac{2\sqrt{\ln 2}F}{\sqrt{\pi}t_p}. \tag{1}$$

Therefore, the intensity distribution of the laser pulse on the crater surface S2 is calculated by $I_{S2}(t) = I(t) \cdot \cos\theta_i$. When the incident angle θ_i equals to 0 deg, i.e., the normal incidence, the intensity distribution measured on the surface S2 is the same as that measured on the surface S1. When the incident angle θ_i reaches 90 deg, i.e., the grazing incidence, the effective laser intensity measured on the surface S2 is much smaller than that measured on the surface S1 and may even be reduced to be less than the threshold intensity for laser ablation. A loose focusing of the laser beam is used, so we neglect the change of the beam size when the laser beam is propagating in the crater cavity.

The primary ablation happens on the crater surface S2. The time-dependent refractive index and reflectivity in the primary ablation are dependent on the free-electron density and denoted by $n_r(t)$ and $R(t)$, respectively. The intensity distribution of the reflected laser pulse is measured on the surface S2 and given by

$$I_{S2R}(t) = I_{S2}(t) \cdot R(t). \tag{2}$$

If we measure the reflected laser beam on the surface S3, which is perpendicular to the beam axis as shown in Fig. 1, the intensity distribution becomes

$$I_r(t) = \frac{I_{S2R}(t)}{\cos\theta_i}. \tag{3}$$

As shown in Fig. 1, when the reflected laser pulse is incident on the sloped crater wall S4 with an incident angle of θ_{ri}, the effective laser intensity can be calculated by

$$I_{SDA}(t) = I_r(t) \cdot \cos\theta_{ri}. \tag{4}$$

If the reflection on the surface S2 is very strong, a larger portion of the incident pulse energy will be reflected. Thus, the reflected pulse may be able to ablate the dielectric material on the surface S4, that is, SDA will occur. The time-dependent free-electron density on the dielectric surface S4 induced by the reflected pulse is denoted by $\rho_r(t)$ and its maximum value during SDA is recorded as ρ_{rm}. The critical free-electron density $\rho_{crit} = (\omega^2 m_e \varepsilon_0)/e$ is used as the criteria for laser ablation,[4,9,13,17] where ω is the laser angular frequency, m_e is the electron mass, ε_0 is the vacuum dielectric permittivity, and e is the electron charge. Therefore, the ablation crater will be formed where the plasma density is larger than the critical value ρ_{crit}.

As our sample, biomaterials are investigated and thus the parameters of water are used to study the plasma formation, as in Ref. 17. Water can be modeled as an amorphous dielectric with band-gap energy of 6.5 eV.[18] Laser pulse of 10 ps at a wavelength of 800 nm is used. The refractive index n_0 of water is 1.33 at 800 nm. In this case, the critical free-electron density for laser ablation is calculated to be $\rho_{crit} = 1.75 \times 10^{21}$ cm^{-3}. Although the biomaterial is used as the sample of transparent dielectrics, the qualitative conclusions of this study could also be applicable for typical transparent dielectrics, such as glass.

3 Fresnel-Drude Model

In laser ablation of transparent dielectrics, the temporal evolution of free-electron density $\rho(t)$[9,11–13] is described by a rate equation.

$$\frac{\partial\rho(t)}{\partial t} = \sigma(t) + \alpha_c(t)I(t)\rho(t) - \eta_{rec}\rho(t)^2, \tag{5}$$

where the terms on the right side are the rates for MPI,[19] CI,[9] and recombination, respectively. At the laser wavelength of 800 nm, the photon energy is 1.56 eV, so five photons are required for MPI. The expressions for the MPI coefficient $\sigma(t)$ and the CI coefficient $\alpha_c(t)$ are given in the Appendix. The recombination coefficient of water[20] is $\eta_{rec} = 2 \times 10^{-9}$ cm^3/s.

The complex dielectric function ε of the ionized dielectrics is a function of the laser-induced free-electron density and given by the Drude model.[12,13]

$$\varepsilon(t) = \varepsilon_r - \frac{\rho(t) \cdot e^2}{m_e\varepsilon_0\omega^2}\frac{\omega\tau}{\omega\tau + i}, \tag{6}$$

where $\varepsilon_r = n_0^2$ is the initial dielectric function, and $\tau = 3.3$ fs is the time between collisions of the electrons with heavy particles in water.[17] The real part of the complex refractive index is time-dependent and given by

$$n_r(t) = \mathrm{Re}\{[\varepsilon(t)]^{1/2}\}. \tag{7}$$

A step-density profile of laser-induced plasma and a sharp air-plasma interface[12–14] are assumed and no plasma expansion[10] happens within the ultrashort pulse. Therefore, the reflectivities for s- and p-polarized light on the air-plasma interface are calculated with the Fresnel equations.[12–15]

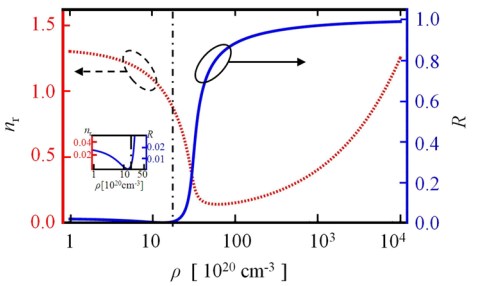

Fig. 2 The refractive index (dashed curve) and the reflectivity (solid curve) of laser-irradiated biomaterial as functions of the free-electron density for the irradiation wavelength of 800 nm at $\theta_i = 0$ deg. The dot-dashed line denotes the position of the critical electron density ρ_{crit}. The inset shows the initial drop of the reflectivity R when increasing the free-electron density.

$$R_s = \left| \frac{n_a \cos\theta_i - \sqrt{\varepsilon}\cos\theta_t}{n_a \cos\theta_i + \sqrt{\varepsilon}\cos\theta_t} \right|^2$$
$$R_p = \left| \frac{n_a \cos\theta_t - \sqrt{\varepsilon}\cos\theta_i}{n_a \cos\theta_t + \sqrt{\varepsilon}\cos\theta_i} \right|^2, \quad (8)$$

where $n_a = 1$ is the refractive index of air, θ_i is the angle of incidence, and θ_t is the angle of refraction calculated by Snell's law, $n_r \sin\theta_t = n_a \sin\theta_i$.

Equations (6) to (8) show that the refractive index n_r and the reflectivity R are functions of the free-electron density,[21,22] which are shown in Fig. 2. When increasing the free-electron density, there are two different regions for the tendency of the refractive index n_r. In the first region where the free-electron density is $<4\times10^{21}$ cm^{-3} (about twice of ρ_{crit}), the refractive index n_r decreases and the slope of the curve gets larger and larger. The minimal value for n_r is ~0.15. In the second region where the free-electron density is $>4\times10^{21}$ cm^{-3}, the refractive index n_r increases slowly. When increasing the free-electron density, the tendency of the reflectivity R is similar with that of the refractive index, i.e., first decreasing and then increasing. But the reflectivity decreases slowly to a minimal value and then drastically rises to a large value of ~0.9. When the refractive index n_r equals to n_a, the reflectivity approaches zero, which can be easily derived from Eq. (8). Therefore, the refractive index and the reflectivity of the ionized dielectrics are both determined by laser-induced free-electron density.

4 Ultrafast Reflection and Secondary Ablation

With the Fresnel-Drude model, in this section, we study the plasma dynamics, ultrafast reflection, and SDA in two cases. In the normal incidence case (Sec. 4.1), the results at different laser fluences are compared and discussed. In the oblique incidence case (Sec. 4.2), the influence of the incident angle θ_i on the temporal dynamics of ultrafast reflection and the SDA is analyzed. With the results in Sec. 4.2, we drew the angular reflectivity curves for different laser fluences and laser polarizations, which are investigated in Sec. 4.3.

With the critical density ρ_{crit} as the ablation criterion, the threshold fluence of the primary laser ablation is calculated to be $F_{th} = 16.9$ J/cm^2 in water with our model, which has a good agreement with the experimental result reported in Ref. 17.

4.1 *Normal Incidence*

The temporal evolutions of the free-electron density ρ, reflectivity R, and reflected pulse intensity I_r in the primary ablation are analyzed at the incident angle $\theta_i = 0$ deg for three fluences ($F = 0.95\,F_{th}$, $1.2\,F_{th}$, and $5\,F_{th}$), as shown in Figs. 3(a) to 3(c). The laser fluence has a great influence on them.

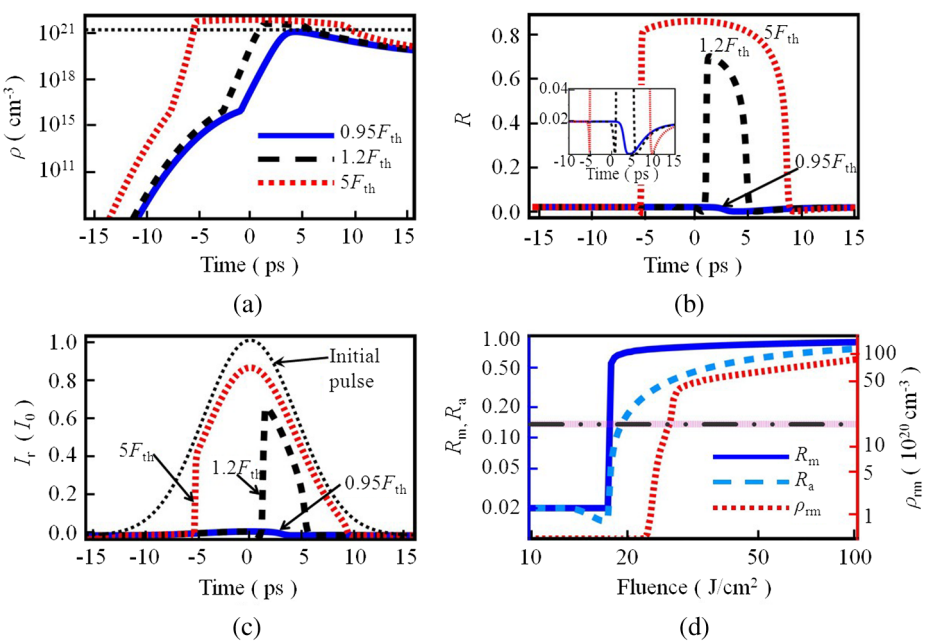

Fig. 3 Time-resolved free-electron density (a), reflectivity (b), and reflected pulse intensity (c) at $\theta_i = 0$ deg and $F = 0.95\,F_{th}$, $1.2\,F_{th}$, and $5\,F_{th}$. (d) The peak and average reflectivities and the peak plasma density of secondary ablation (SDA) as functions of laser fluence. The horizontal lines in (a) and (d) indicate the position of ρ_{crit}.

The evolution of the free-electron density induced by the laser pulse with different fluences has the similar quality as shown in Fig. 3(a). At the beginning of the pulse, only MPI dominates to generate free electrons. When the free-electron density is increased to $\sim 10^{16}$ cm^{-3} by MPI, steep increase of the free-electron density is observed and turning points are formed on the three curves for different laser fluences in Fig. 3(a). The reasons are that CI dominates in the free-electron generation at the densities $>10^{16}$ cm^{-3} and also the CI rate is much larger than the MPI rate. For laser pulse with the fluence of $5\,F_{\text{th}}$, the turning point happens much earlier, and the duration of the high-density region where $\rho > \rho_{\text{crit}}$ is >10 ps.

Figure 3(b) shows the temporal evolution of the reflectivity on the surface S2 irradiated by laser pulse with the three fluences. As shown in Fig. 2 and discussed in Sec. 3, when increasing the free-electron density, the reflectivity initially decreases slowly to a minimal value and then drastically rises to a large value of ~0.9. When the laser fluence F is $0.95\,F_{\text{th}}$, the maximum free-electron density is smaller than the critical value ρ_{crit}. Before $t = 5$ ps, the free-electron density increases with time and thereby the reflectivity R decreases to 0; after $t = 5$ ps, because of the relaxation of the free-electron density, the reflectivity R increases with time. When the laser fluence $F > F_{\text{th}}$, the reflectivity drops to almost 0 and then rises to a large value in a very short time when the free-electron density exceeds the critical value ρ_{crit}. The duration of high reflectivity ($R > 0.6$) shown in Fig. 3(b) is determined by that of the free-electron density above the critical value shown in Fig. 3(a). For higher laser fluence, the duration of high reflectivity ($R > 0.6$) is larger, as shown in Fig. 3(b). It is ~14 ps at the laser fluence of $5\,F_{\text{th}}$.

With Eq. (3) and the data in Fig. 3(b), we calculated the intensity distribution of the reflected pulses for three different laser fluences. When the laser fluence $F > F_{\text{th}}$, the intensity distribution $I_{\text{r}}(t)$ of the reflected pulse is a Gaussian-like shape with a cut-off front ramp [see Fig. 3(c)]. When $F = 5\,F_{\text{th}}$, the main part of the laser pulse is reflected and the reflected pulse has almost the same width as the original pulse. Most of the laser pulse energy is carried by the reflected laser pulse in the primary ablation and it is enough to induce a second ablation.

The time-averaged reflectivity R_{a} at the center of the focal spot[11] is defined by

$$R_{\text{a}} = \frac{\int I_{\text{S2}}(t)\mathrm{d}t}{\int I(t)\mathrm{d}t}. \tag{9}$$

We calculated the peak reflectivity R_{m} and average reflectivity R_{a} as functions of laser fluence, which are shown in Fig. 3(d). When $F < F_{\text{th}}$, the peak reflectivity equals to 0.02 and the average reflectivity R_{a} drops below 0.03 with increasing laser fluence. When laser fluence reaches F_{th}, the peak reflectivity R_{m} dramatically rises up to 0.8 and the average reflectivity R_{a} increases continuously. Therefore, the average reflectivity is a good quantity to describe the strength of the reflection.

Since the laser pulse is at normal incidence in the primary ablation, the reflected beam is overlapped with the original beam but propagates in the opposite direction. Therefore, it is impossible to induce a secondary reflection. In order to demonstrate the strength of the reflected pulse, however, it is still assumed that the reflected pulse shown in Fig. 3(c) is normally incident on the crater wall. In this case, the threshold fluence of the initial pulse for SDA is minimal. The peak free-electron density ρ_{rm} of SDA has been calculated as a function of laser fluence as shown in Fig. 3(d). The threshold fluence for SDA at $\theta_{\text{ri}} = 0$ deg is found to be 32 J/cm^2, which is almost twice of that for the primary ablation.

4.2 *Oblique Incidence*

In laser processing, as the sidewall of the ablation crater gets steeper when increasing the pulse number, for the subsequent pulse, the angle of incidence could increase from 0 up to 85 deg.[6–8] In this section, we study the influence of the incident angle θ_{i} on the dynamics of the plasma generation and ultrafast reflection in the primary ablation as well as the plasma dynamics of the SDA in the case of laser fluence $F = 5\,F_{\text{th}}$. The sampling values of the incident angle θ_{i} are taken from 0 to 90 deg with an interval of 5 deg. $\theta_i = 0$ deg indicates the normal incidence, which has been discussed in the last section. $\theta_i = 90$ deg represents the case that the original laser pulse directly interacts with the dielectric surface S4 without the primary ablation.

The angular dependences of the electron density ρ and the reflectivity R in the primary ablation with a fluence of $5\,F_{\text{th}}$ are presented in Figs. 4(a) to 4(c). The effective fluence $F\cos\theta_{\text{i}}$ on the surface S2 decreases continuously with θ_{i} increasing due to the projection on the sloped sidewall. Therefore, as shown in Fig. 4(a), the peak electron density drops with θ_{i} increasing. When $\theta_{\text{i}} > 70$ deg, the projected fluence is lower than F_{th} and the primary ablation does not occur. It is easily found that there is a big gap between the two curves for the angles of 55 and 60 deg in Fig. 4(a), and the angle corresponding to the gap is determined by the free-electron density. As shown in Fig. 2, when the free-electron density increases beyond 2×10^{21} cm^{-3}, the refractive index $n_{\text{r}}(t)$ drastically decreases to be the minimal value of 0.15. As described by Eq. (11), the CI coefficient is inversely proportional to the refractive index $n_{\text{r}}(t)$, and thereby the CI rate increases by one order of magnitude. Therefore, when the incident angle is >55 deg, the maximum of free-electron density drops to be around the critical density because of the larger refractive index and the smaller CI rate.

The angle of incidence has a significant influence on the transient reflectivity R in the primary ablation, as shown in Fig. 4(b). When the incident angle θ_i is in the range of 0 to 55 deg, the plasma reflection is very strong and the peak reflectivity reaches 0.8. The duration of high reflectivity is decreasing with increase of the incident angle. When $\theta_{\text{i}} > 60$ deg, the Fresnel reflectivity increases, while the contribution of plasma reflection decreases. When $\theta_{\text{i}} = 75$ deg, the reflectivity R approaches to zero at $t = 5$ ps because of $\rho \approx \rho_{\text{crit}}$. When $\theta_{\text{i}} > 75$ deg, the laser-induced free-electron density ρ is too small to affect the reflectivity and the Fresnel reflection dominates in the reflection behaviors. There is a drop for the curve of the reflectivity R at the beginning of the pulse and it is much clearer at large angles of incidence. The reason for this drop is the same as that in Fig. 3(b). That is, when the free-electron density increases, the reflectivity first drops and then drastically rises.

The temporal evolution of the laser intensity I_{r} of the reflected pulses measured on the surface S3 at different angles of incidence is shown in Fig. 4(c). Three regions

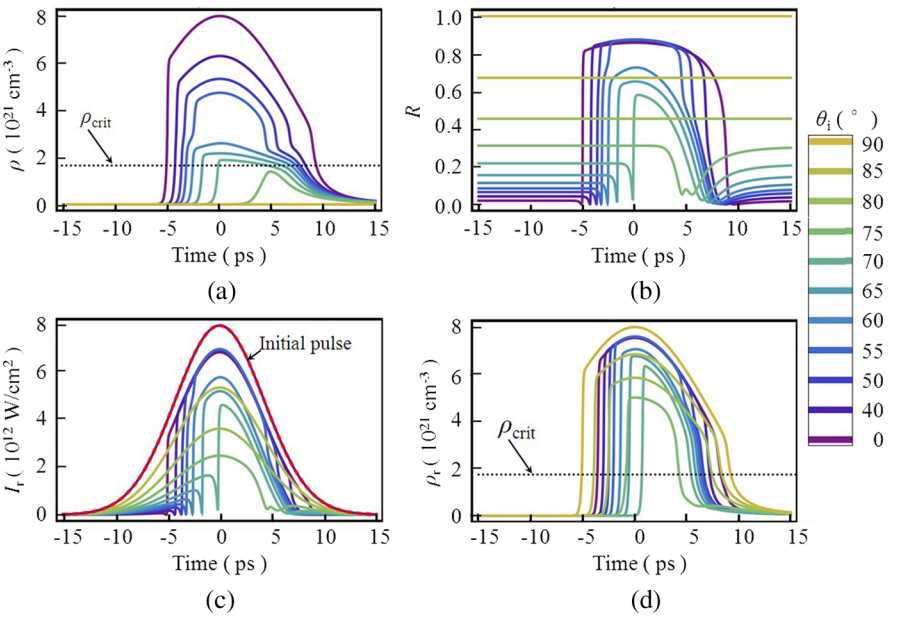

Fig. 4 Temporal dynamics of free-electron density (a), reflectivity (b), reflected pulse intensity (c), and free-electron density of SDA (d) at various angles of incidence. An s-polarized, 5 F_{th}, 10 ps, 800 nm pulse is used. The intensity distribution of the initial pulse is measured on the surface S1.

of the incident angle corresponding to the reflection mechanism can be distinguished. When the incident angle $\theta_i \leq 55$ deg, the laser pulse itself induces a significant reflection due to the generation of free electrons. Since the high-reflectivity region almost covers the main part of the incident laser pulse [see Fig. 4(b)], the intensity distributions of the reflected pulses have Gaussian-like temporal profiles with cut-off front ramps. When the incident angle θ_i is in the range of 60 to 70 deg, laser-induced free-electron density gets slightly larger than the critical density ρ_{crit}. Therefore, from Fig. 2, we can know that the effect of the plasma gas on the reflectivity is comparable to that of the Fresnel reflectivity. The amplitude and width of the reflected pulses are both reduced because of the lower reflectivity. The drop of the intensity at the beginning of the laser pulse is caused by the reflectivity characteristics shown in Fig. 3(b). When the incident angle θ_i is >75 deg, i.e., the grazing incidence, the Fresnel reflectivity rises to be >0.3, while the reflectivity induced by the free-electron density is negligible due to the low effective fluence.

If the reflected laser pulse in Fig. 4(c) is at normal incidence on the crater sidewall again, i.e., the incident angle $\theta_{ri} = 0$ deg, the free-electron dynamics of SDA is described in Fig. 4(d). The peak free-electron densities ρ_{rm} induced by the reflected pulse exceed the ablation threshold at any incident angle of θ_i; thus the SDA behavior is extremely significant. Keep in mind that the effective intensity I_{SDA} is calculated by Eq. (4) with the reflected pulse intensity I_r in Fig. 4(c). Thus, the effective intensity on the surface S4 could be larger than that on the surface S2, especially at large incident angles of θ_i. Comparing Figs. 4(a) and 4(d), when $\theta_i > 60$ deg, the free-electron density generated in SDA is even larger than that of the primary ablation.

We have also obtained the corresponding results for the p-polarized pulse, which are quite similar with those for the s-polarized pulse in Fig. 4. The comparison of the averaged reflectivity between s- and p-polarized pulses will be given in the following section.

4.3 *Angular Reflectivity Curve*

With Eq. (9) and the results in Fig. 4, we have studied the angular dependence of average reflectivity, so-called angular reflectivity curve, of the dielectric surface S2 excited by s- and p-polarized laser pulses with different fluences ($F = 0\,F_{th}$, $1.2\,F_{th}$, $2\,F_{th}$, $5\,F_{th}$). They are compared with the usual Fresnel reflectivity curves in Fig. 5(a).

In Fig. 5(a), $0\,F_{th}$ indicates the curves for the low-fluence limit, and the Fresnel formula leads to the characteristic reflectivity curves[15] for s- and p-polarized light. For the cases of laser fluence larger than the threshold fluence (i.e., $F = 1.2\,F_{th}$, $2\,F_{th}$, $5\,F_{th}$), the average reflectivity R_a of the laser-excited dielectric surface depends on the polarization, angle of incidence, and laser fluence. We found that the angular reflectivity curve for s-polarized pulse (s-curve) is slightly different from that for p-polarized pulse (p-curve). For example, they are crossing each other at some angle between $\theta_i = 20$ and 80 deg, while s-curve is always above p-curve in the low-fluence limit. Moreover, the effect of the Brewster angle on the p-curve is covered by the plasma reflectivity.

For the limit of vanishing fluence, the well-known Fresnel reflectivity curves (i.e., low-fluence limit) are well reproduced. For the other three laser fluences, the angular reflectivity curves in Fig. 5(a) have the similar characteristics, but a larger fluence leads to a greater reflectivity. The reflectivity R_a at small angles of incidence decreases slightly with increase in θ_i. This agrees well with the experimental observations that smaller reflectivities have been found for larger angles of incidence in the experiments of various target materials.[10] When the incident angle θ_i is large enough, the effective laser fluence on the sloped surface is smaller than F_{th} and laser-induced free-electron density has a minimal effect

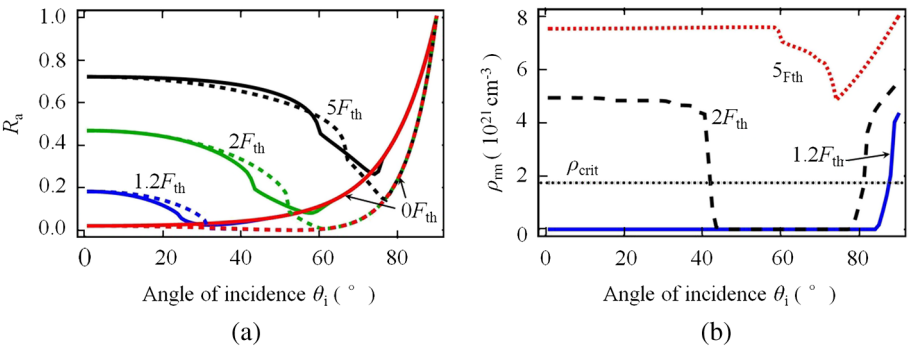

Fig. 5 (a) Angular dependence of reflectivity on the dielectric surface S2 for s- (solid) and p- (dashed) polarized pulses. (b) The peak free-electron density of SDA on the dielectric surface S4 for s-polarized pulses as a function of the incident angle θ_i. The incident angle of the reflected pulse on the surface S4 is fixed to $\theta_{ri} = 0$ deg.

on the reflectivity. Thus, the angular reflectivity curves coincide with those in the low-fluence limit at a certain angle θ_c. The angle θ_c is the characteristic angle at which the effect of the plasma density on the reflection vanishes. The angle θ_c grows with the laser fluence and is ~75 deg for $5\,F_{th}$, which means that the angle region where the plasma reflection is dominant in the surface reflection expands.

As described in Fig. 4(d), the free-electron density of SDA on the surface S4 strongly depends on the incident angle θ_i of the primary ablation. The angular dependences of the peak density ρ_{rm} at $\theta_{ri} = 0$ deg for s-polarized pulse with different fluences are shown in Fig. 5(b). Comparing the peak density ρ_{rm} with the critical density for laser ablation, we obtained the SDA regions of the incident angle θ_i. For the fluence of $1.2\,F_{th}$, there are SDA behaviors only when $\theta_i > 80$ deg. For the fluence of $2\,F_{th}$, SDA happens in two regions of the incident angle, i.e., $\theta_i < 40$ deg and $\theta_i > 80$ deg. For the fluence of $5\,F_{th}$, SDA can occur at any value of θ_i, while the ablation strength of the reflected pulse gets minimal at $\theta_i = 75$ deg.

5 Road Map to Secondary Ablation

In the above studies of SDA, the normal incidence of the reflected pulse is always assumed ($\theta_{ri} = 0$ deg). In the experiments, however, θ_{ri} can be arbitrary between 0 and 90 deg due to the uncertainty of the crater shape. Therefore, we calculated the peak free-electron density ρ_{rm} at different incident angles of θ_i and θ_{ri} ranging from 0 to 90 deg. Drawing the contour of the peak free-electron density ρ_{rm} corresponding to the critical value ρ_{crit} for laser ablation, we obtained a map of SDA on the incident angles of θ_i and θ_{ri} for s-polarized laser pulse with different fluences ($F = 1.2\,F_{th}$, $2\,F_{th}$, $3\,F_{th}$, $4\,F_{th}$, and $5\,F_{th}$) as shown in Fig. 6. The curves on the map indicate the boundaries between the SDA region and the non-SDA region for the corresponding fluences. The area below each curve stands for the presence of SDA. For the fluence of $1.2\,F_{th}$, SDA happens only when the original pulse provides glancing incidence ($\theta_i > 85$ deg) and the incident angle $\theta_{ri} < 30$ deg. For the fluence of $2\,F_{th}$ to $4\,F_{th}$, the SDA area consists of two regions on the map. The near rectangular area in the lower left corner is because of high reflectivity of laser-induced plasma. The near triangular area in the lower right corner is due to the high reflectivity at larger angles of incidence. The $5\,F_{th}$ curve is continuous, and therefore, SDA could happen at any incident angle of θ_i, while the second incident angle of θ_{ri} has a limit range of 45 to 70 deg. The map of SDA for p-polarized pulses had also been drawn and is similar with that for s-polarized pulses, and therefore not given here. Their comparison shows that Brewster angle is not the explanation for the non-SDA region at the incident angle θ_i of ~70 deg, which can also be concluded from Fig. 5(a).

From the map of SDA, we found two mechanisms to support the reflected pulse and thereby induce SDA. For smaller angles of the first incidence, the ultrafast reflectivity induced by laser-excited plasma is dominant in the reflection behaviors. For the larger angle θ_i of the first incidence, the effective fluence is below the ablation threshold and high reflectivity calculated from the common Fresnel equation is the main cause of the strong reflection.

The map of SDA shows that SDA is essential in laser cutting and drilling of transparent dielectrics with high-fluence pulses. The SDA on the crater sidewall results in material removal and some of microcracks beneath the sidewall,[4] and these have been observed in the experiment.[5,7] In the SDA on the crater sidewall, the energy deposition of the laser pulse on the surface leads to material removal and thereby additional small craters. Meanwhile, laser refraction and

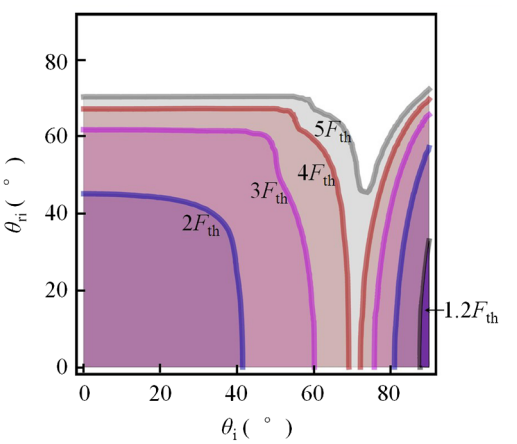

Fig. 6 Map of SDA on the incident angles of θ_i and θ_{ri} for an s-polarized pulse with various laser fluences. The area below the curves is the SDA region for the corresponding fluence.

diffraction dominate in the intensity distribution of the transmitted laser beam,[4] and the transmitted laser intensity is absorbed and high-density free electrons are generated beneath the crater wall. Some long needle-like damage tracks are formed in the region where laser-induced free-electron density is above the damage threshold.[4] These damages under the surface are possible sources of microcrack formation in the subsequent processing. However, there are other possible causes for the microcracks, such as the thermal stress,[23] and the exact role of SDA in microcrack formations can be determined and verified by the relevant experiments. Besides, the saturation of the processing depth can be overcome because of SDA. Due to the arbitrary incident direction of the reflected pulse in SDA, the drilling direction can be changed in the ultrashort pulsed laser drilling process.[7,8] Multiple reflections in laser channeling can also be studied by applying the map of SDA repeatedly.

The map of SDA also provides a way to avoid SDA and optimize the laser processing procedure. For $F < 5\,F_{\mathrm{th}}$, there is a non-SDA region of the incident angle θ_{i}. For $F = 5\,F_{\mathrm{th}}$, when $\theta_{\mathrm{i}} = 75$ deg, the limit for the angle θ_{ri} is smallest to induce SDA. In laser processing scheme shown in Fig. 1, we can search the non-SDA area for a given value of θ_{i} on the map in Fig. 6. By controlling the angles of incidence, SDA can be avoided or reduced, and thereby the microcracks[5] in laser micromachining can be reduced. In this study, only the reflection at the spot center of the laser beam is considered. If the transverse intensity distribution of the laser beam is a perfect Gaussian profile, the ablation occurs first at the spot center where the peak intensity is located; thus the map of SDA shown in Fig. 6 can be applied in the real experiments. Otherwise, the exact intensity distribution of the laser beam on the transverse plane must be taken into account in applying the model and getting the map of SDA. Meanwhile, for any crater shape, the map of SDA can be applied in laser processing as long as the incident angles in the primary and secondary ablations are given.

6 Conclusion

The time-dependent refractive index significantly affects the CI rate and thereby the temporal dynamics of laser-induced free-electron density. Despite the Fresnel reflection, the laser pulse itself can induce a significant reflection due to the generation of free electrons. However, they play different roles in the reflection behaviors at different angles of incidence. At a laser fluence above the ablation threshold, for smaller angles of the first incidence, the ultrafast reflectivity induced by laser-excited plasma is dominant in the reflection behaviors; for the larger angle θ_{i} of the first incidence, the effective fluence is below the ablation threshold and the Fresnel reflectivity determines the intensity of the reflected pulse. The laser-induced plasma and large angle of incidence both produce a great reflectivity and thereby, could lead to the SDA phenomenon. The angular reflectivity curves of the laser-excited dielectric surface significantly differ from those for the low-fluence limit in the range of lower incident angles, and they coincide when the incident angle is large enough to lower the effective fluence below the ablation threshold. The map of SDA on the angles of the first and second incidences for various fluencies shows the regions where SDA may happen. The SDA theory gives rise to the explanations for overcoming the saturation of the ablation crater depth and inducing microcracks underneath the ablation crater wall, which are critical issues in ultrashort laser processing.

Appendix: Parameters in Rate Equation

The parameters in the rate equation [Eq. (5)] for free-electron density are given here.

Multiphoton ionization coefficient: The expression of multiphoton ionization coefficient σ is taken as the approximated expressions derived by Keldysh[19] and given by

$$\sigma(t) = \frac{2\omega}{9\pi}\left(\frac{m\omega}{\hbar\gamma\Gamma}\right)^{3/2} Q\left(\gamma, \frac{E_{\mathrm{g}}}{\hbar\omega}\right) \exp\left\{-\left\langle \frac{E_{\mathrm{g}}}{\hbar\omega} + 1\right\rangle \Xi\right\}, \tag{10}$$

where

$$Q(\gamma, x) = \sqrt{\pi/2K(\Gamma)} \sum_{l=0}^{\infty} \exp\{-l\Xi\} \times \Phi\{[\pi(2\langle x+1\rangle - 2x + l)/2K(\Gamma)E(\Gamma)]^{1/2}\},$$

$$\Xi = \pi[K(\gamma\Gamma) - E(\gamma\Gamma)]/E(\Gamma), \quad \Gamma = \frac{1}{\sqrt{1+\gamma^2}},$$

$$\gamma = \frac{\omega}{e}\sqrt{\frac{c\varepsilon_0 m E_{\mathrm{g}}}{4I(t)}}.$$

Here $\langle x\rangle$ represents the integer part of the number x, $K()$ and $E()$ denote elliptic integrals of the first and second kinds, and $\Phi()$ denotes the Dawson probability integral. m is the exciton reduced mass and c is the light speed in vacuum.

Cascade ionization coefficient: The generated free electron by MPI absorbs energy by inverse bremsstrahlung absorption, and it will produce a new free electron when its kinetic energy reaches the critical energy $E_{\mathrm{crit}} = 1.5\,E_{\mathrm{g}}$.[9] The CI coefficient[9] is given by

$$\alpha_{\mathrm{c}}(t) = \frac{1}{\omega^2\tau^2 + 1}\frac{e^2\tau}{cn_{\mathrm{r}}(t)\varepsilon_0 m_{\mathrm{e}} E_{\mathrm{crit}}}. \tag{11}$$

Acknowledgments

This research is supported by the Fraunhofer-Gesellschaft-Chinese Academy of Sciences Joint Doctoral Promotion Program and funding from the Fraunhofer Institute for Laser Technology.

References

1. R. R. Gattass and E. Mazur, "Femtosecond laser micromachining in transparent materials," *Nat. Photon.* **2**(4), 219–225 (2008).
2. G. D. Valle, R. Osellame, and P. Laporta, "Micromachining of photonic devices by femtosecond laser pulses," *J. Opt. A: Pure Appl. Opt.* **11**(1), 013001 (2009).
3. S. Nolte et al., "Cutting of optical materials by using femtosecond laser pulses," *Proc. SPIE* **4440**, 152–160 (2001).
4. M. Sun et al., "Numerical analysis of laser ablation and damage in glass with multiple picosecond laser pulses," *Opt. Express* **21**(7), 7858–7867 (2013).
5. H. Varel et al., "Micromachining of quartz with ultrashort laser pulses," *Appl. Phys. A* **65**(4–5), 367–373 (1997).
6. S. Darvishi, T. Cubaud, and J. P. Longtin, "Ultrafast laser machining of tapered microchannels in glass and PDMS," *Opt. Laser Eng.* **50**(2), 210–214 (2012).

7. S. Doering et al., "In situ imaging of hole shape evolution in ultrashort pulse laser drilling," *Opt. Express* **18**(19), 20395–20400 (2010).
8. S. Doering et al., "Evolution of hole depth and shape in ultrashort pulse deep drilling in silicon," *Appl. Phys. A* **105**(1), 69–74 (2011).
9. A. Vogel et al., "Mechanisms of femtosecond laser nanosurgery of cells and tissues," *Appl. Phys. B* **81**(8), 1015–1047 (2005).
10. Ch. Ziener et al., "Specular reflectivity of plasma mirrors as a function of intensity, pulse duration, and angle of incidence," *J. Appl. Phys.* **93**(1), 768–770 (2003).
11. G. Doumy et al., "Complete characterization of a plasma mirror for the production of high-contrast ultraintense laser pulses," *Phys. Rev. E* **69**(2), 026402 (2004).
12. A. Q. Wu, I. H. Chowdhury, and X. Xu, "Femtosecond laser absorption in fused silica: numerical and experimental investigation," *Phys. Rev. B* **72**(8), 085128 (2005).
13. L. Jiang and H.-L. Tsai, "A plasma model combined with an improved two-temperature equation for ultrafast laser ablation of dielectrics," *J. Appl. Phys.* **104**(9), 093101 (2008).
14. T. E. Itina and N. Shcheblanov, "Electronic excitation in femtosecond laser interactions with wide-band-gap materials," *Appl. Phys. A* **98**(4), 769–775 (2010).
15. M. Born and E. Wolf, *Principle of Optics*, Cambridge University Press, Cambridge (1999).
16. N. N. Nedialkov and P. A. Atanasov, "Molecular dynamics simulation study of deep hole drilling in iron by ultrashort laser pulses," *Appl. Surf. Sci.* **252**(13), 4411–4415 (2006).
17. M. D. Feit, A. M. Komashko, and A. M. Rubenchik, "Ultra-short pulse laser interaction with transparent dielectrics," *Appl. Phys. A* **79**(7), 1657–1661 (2004).
18. F. Williams, S. P. Varma, and S. Hillenius, "Liquid water as a lone-pair amorphous semiconductor," *J. Chem. Phys.* **64**(4), 1549–1554 (1976).
19. L. V. Keldysh, "Ionization in the field of a strong electromagnetic wave," *Soviet Phys. JETP* **20**(5), 1307–1304 (1965).
20. F. Docchio, "Lifetimes of plasmas induced in liquids and ocular media by single Nd:YAG laser pulses of different duration," *Europhys. Lett.* **6**(5), 407–412 (1988).
21. D. Puerto et al., "Dynamics of plasma formation, relaxation, and topography modification induced by femtosecond laser pulses in crystalline and amorphous dielectrics," *J. Opt. Soc. Am. B* **27**(5), 1065–1076 (2010).
22. S. Hoehm et al., "Femtosecond laser-induced periodic surface structures on silica," *J. Appl. Phys.* **112**(1), 014901 (2012).
23. I. Miyamoto, K. Cvecek, and M. Schmidt, "Crack-free conditions in welding of glass by ultrashort laser pulse," *Opt. Express* **21**(12), 14291–14302 (2013).

Mingying Sun is currently working in Shanghai Institute of Optics and Fine Mechanics, Chinese Academy of Science. From November 2010 to February 2013, he worked as a research assistant in the Department of Modelling and Simulation of Fraunhofer Institute for Laser Technology. His fields of interest are in the modeling and simulation of ultrashort pulsed laser ablation in transparent dielectrics, as well as the analysis and simulation of laser resonators.

Biographies for other authors are not available.